

# A Dual-Mesh Microwave Reconstruction Method Based on Compressive Sampling Matching Pursuit Algorithm

Huiyuan Zhou and Ram M. Narayanan\*

**Abstract**—In this paper, the Compressive Sampling Matching Pursuit Algorithm (CoSaMP) is applied to microwave reconstruction of a 2-dimensional non-sparse object. First, an adaptive discretization method, DistMesh method, is applied to discretize the image domain based on the region of interest. The dual-mesh method is able to provide denser and smaller discretized cells in more important areas of the object and larger cells in other areas, thereby providing more details in the interest domain and keeping the computational burden at a reasonable level. Another benefit of using the dual-mesh method is that it automatically generates size functions and adapts to the curvature and the feature size of the geometry. In addition, the size of each cell changes gradually. Next, the inverse scattering problem is solved in frame of Distorted Born Iterative Method (DBIM). During each iteration of DBIM, the near field scattering problem is modeled as a set of linear equations. Furthermore, a compressive sensing (CS) method called the Compressive Sampling Matching Pursuit Algorithm is applied to solve the nonlinear inverse problem. During this process, two innovative steps are applied. First, for the reconstruction of the non-sparse object, the signal input to our algorithm is processed via a wavelet transformation to obtain sparsity. Second, as the dual-mesh method discretizes more important cells in smaller sizes, these cells have high potential to be filtered by the threshold of CoSaMP. As a result, a regularization matrix is introduced to reduce the effect of size. Finally, we present numerical experiment results based on our dual-mesh method combined with the regularized CoSaMP algorithm.

## 1. INTRODUCTION

Microwave image reconstruction arises in various engineering applications, such as medical imaging [1], ground penetration radar detection, and other non-invasive testing [2, 3]. The main challenge for microwave reconstruction algorithms stems from the nonlinear and ill-posed properties of the problem [4]. For the microwave inverse imaging problem, the estimation of permittivity and conductivity from the object can provide information for further application and processing.

Recently, various inversion algorithms have been developed to obtain stable and robust reconstruction results. At the early stage, conventional optimization methods are fully developed to be applied to microwave imaging, such as Gauss-Newton (GN) optimization algorithms [5–7], conjugate gradient methods [8, 9], and level set methods [10, 11]. Recently, algorithms inspired by compressed sensing (CS) theory [12], which have been developed for efficient reconstruction of sparse signals in image processing applications, have garnered more attention and gained popularity. Before its application to microwave imaging, CS methods have been widely developed and applied in signal and image processing applications, as they are able to recover a sparse signal from a lower dimensional measurement, i.e., the number of measurements is much less than the number of signal entries. These compressive sensing methods, known as sparsity regularization techniques, are currently becoming more popular in microwave imaging research.

---

*Received 2 September 2019, Accepted 15 October 2019, Scheduled 23 October 2019*

\* Corresponding author: Ram M. Narayanan (ram@enr.psu.edu).

The authors are with the Department of Electrical Engineering, The Pennsylvania State University, University Park, PA 16802, USA.

By using different types of thresholding techniques iteratively for the sparse signal, various CS methods have been proposed. There are many possible algorithms that have been developed for recovering an estimate of signal from a small number of measurements, as the orthogonal matching pursuit (OMP) algorithm [13, 14], iterative hard threshold (IHT) algorithm, and iterative method with adaptive thresholding for compressive sensing (IMATCS) [15, 16]. In [17, 18], the iterative hard threshold algorithm is described. Meanwhile, an Iterative Method with Adaptive Thresholding for Compressed Sensing was proposed with adaptive thresholding function at each iteration for the sparse signal input to the algorithm. In addition, compressive sampling matching pursuit (CoSaMP) [19], which is based on OMP, has been developed as a fast algorithm for convex relaxation. The CoSaMP method is able to identify components during each iteration, which makes it work fast on many types of signals.

In this paper, we propose a dual-mesh method to discretize the image domain by applying the Distmesh technique [20]. The majority of microwave reconstruction methods use a uni-mesh method, which leads to the fact that even for the area of non-interest, the discretized cells have the same size as the cells in the region of interest [21, 22]. As a result, for high resolution imaging, the image domain has to be uniquely discretized by small cells in solving the forward problem, which introduces a very heavy computational burden for the algorithms. In addition, the Distmesh discretization method can avoid large variations in element sizes by a mesh size function, which is used to determine the equilibrium lengths of the edges. Compared to the typical Delaunay refinement algorithm, this algorithm forces equilibrium and tends to give much higher values of the mesh quality. The combination of distance function representation and node movements from forces turns out to be good for the dual-mesh scheme of inverse scattering. After applying the dual-mesh method, the smaller cells describe the area where we have more interest and have relatively lower estimated value due to their smaller size. To compensate the size difference and to maintain the efficiency and accuracy of our algorithm, a regularization matrix is introduced before applying the CoSaMP algorithm.

After the discretization of the non-sparse image, a novel wavelet transformation, called the Non-Decimated Wavelet Transformation (NDWT) [23], is applied to obtain sparsity to the 2-dimensional non-sparse object. NDWT has the advantages of time-invariance and redundancy, compared to the standard orthogonal wavelet transformations. In addition, NDWT matrix is able to efficiently map a signal from an acquisition domain to the wavelet domain with simple matrix multiplication and without the requirement of the total number of the signal [24].

In this paper, a new method for applying CoSaMP for the numerical solution of 2-dimensional non-sparse inverse scattering problem is proposed. During the Method of Moment (MoM) process, the non-sparse object is discretized by Distmesh method to obtain robust dual-mesh grid for emphasis and enhancement of the information in the region of interest. Then, the ND-Wavelet (NDW) transformation method is applied to input signal for sparsity in the wavelet domain. Afterwards, we combine the DBIM method and CoSaMP to iteratively recover the sparse signal. In the end, using the inverse ND-wavelet transformation, the final reconstruction results are obtained.

This paper is organized as follows. A review of EM inverse scattering and dual-mesh method for discretization are given in Section 2. The theory of CoSaMP and ND-Wavelet theory are introduced in Section 3. Afterwards, a representative set of results from numerical experiments is presented in Section 4 to assess its accuracy, effectiveness, and efficiency. Finally, some conclusions are reported in Section 5.

## 2. PROBLEM STATEMENT

### 2.1. EM Inverse Scattering Model

In this paper, we propose a method to reconstruct 2-dimensional dielectric profile of non-sparse object. In this section, we briefly introduce the microwave scattering theory and model for 2-dimensional situation for completeness and better understanding.

Generally, for 2-dimensional microwave scattering theory, there are two main methods based on differently polarized incident signals. One is TE polarization, and the other is TM polarization. For computational efficiency and simplicity of model, we choose the TM polarization model. In the TM case, the incident field is set to be a TM-polarized electric field. As shown in Fig. 1, an object with arbitrary cross-section shape is described in 2-D situation. The image in  $x$ - $y$  plane is divided into two

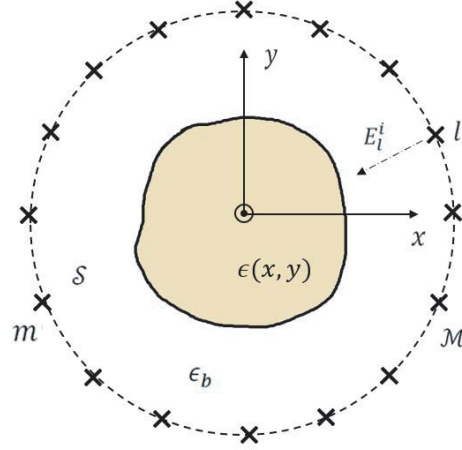


**Figure 1.** Illustration of EM inverse scattering scenario.

domains. The inside part containing the object and surrounding homogeneous background medium is named as the image domain and denoted by  $\mathcal{S}$  in the  $x$ - $y$  plane and oriented along the  $z$ -axis. The outside part including the circularly placed transmitter and receivers is named the measurement domain and denoted as  $\mathcal{M}$ . As we consider a TM polarization problem, the transmitter is modeled by a current source along  $z$ -axis. As shown in Fig. 1,  $M$  antennas are placed at a same radius around the object, denoted as subscript  $m \in [1, M]$ . Each antenna acts as a transmitter sequentially, and the remaining  $M - 1$  antennas act as the receivers simultaneously. We denote the transmitting antenna using subscript  $l \in [1, L]$ . Let  $r(x, y)$  be the coordinates of a spatial point in the imaging domain. We denote the complex permittivity at point  $r(x, y)$  as  $\epsilon(r)$ ,

$$\epsilon(r) = \epsilon'(r) - j\epsilon''(r) = \epsilon_0 \left( \epsilon_r(r) - j \frac{\sigma(r)}{\omega\epsilon_0} \right) \quad (1)$$

where  $\epsilon'$  and  $\epsilon''$  are the real and imaginary parts of dielectric permittivity respectively;  $\epsilon_0$  is the permittivity of free space; and  $\epsilon_r$  is the relative permittivity.

Based on the scalar wave equation and boundary conditions, the scalar electrical field integral equation (EFIE) is given by

$$E_l(r) = E_l^i(r) + \omega^2 \mu \iint_S \Delta\epsilon(r') E_l(r') G^r(r, r') dr' \quad (2)$$

where  $E$  and  $E^i$  are, respectively, the total EM field and incident EM field, and  $\Delta\epsilon(r) = \epsilon(r) - \epsilon_b$  is the unknown contrast permittivity compared with the exterior background medium complex permittivity. Then, the contrast  $\Delta\epsilon(r)$  is given as

$$\Delta\epsilon(r) = \begin{cases} \epsilon(r) - \epsilon_b & \text{if } r \in S \\ 0 & \text{if } r \notin S \end{cases} \quad (3)$$

In Equation (2),  $G^r(r, r')$  is the two dimensional free space Green's function, given by  $G^r(r, r') = (i/4)H_0^{(1)}(k_{\text{ext}}|r - r'|)$  [25]. The scattered field received by the antennas is calculated using

$$E_l^{sc}(s_m) = \omega^2 \mu \iint_S \Delta\epsilon(r') E_l(r') G^s(s_m, r') dr' \quad (4)$$

where  $G^s(s_m, r')$  is Green's function between image domain and measurement domain.

Equations (2) and (4) describe the forward scattering process which is used to calculate the scattered field with the information of the incident field and predicted dielectric properties. The forward problem is computed every time during the inverse iteration process [26]. After discretizing the image domain, the forward problem is able to be presented in discrete form. Equations (2) and (4) are recast as

$$[I - G^r \Delta\epsilon] E_l = E_l^i \quad (5)$$

$$E_l^{sc} = G^s E_l \Delta \epsilon \quad (6)$$

where  $G^r$  is an  $N \times N$  matrix of the integrated Green's functions for incident field and total field on each cell;  $G^s$  is an  $M \times N$  matrix of the integrated Green's function for total field on each cell and scattered field at different receivers; and  $N$  is the total number of the discretized cells. During each iteration, the Green's function is updated by the Distorted Born Iterative method (DBIM) [27].

## 2.2. Dual-mesh Discretization of Object Using DistMesh

Based on the microwave scattering theory described above, the matrix form forward problem is generated and needs to be solved using the computational electromagnetic method. Based on [2], various solving methods are available, as the Finite-Difference Time Domain method (FDTD), Finite Element method (FEM), and Method of Moment (MoM). In this paper, we choose MoM as it easily exploits the matrix form integral relation we introduce above.

Under the scheme of MoM, the imaging domain  $\mathcal{S}$  is discretized in small discrete cells. The center of each cell is chosen as the position of the entire cell.

Conventionally, the object is discretized in rectangular uni-size cells. As shown in Fig. 2, in the rectangular mesh scheme, the mesh grid is not able to align along the boundary of image domain. In addition, in the dual-mesh situation, the denser mesh grid changes sharply. As the result, in this paper, for enhanced resolution in the interest area, we apply the Distmesh method, a kind of triangular discretized method. Its advantages, compared to the traditional rectangular mesh grid, are that the image domain changes along the boundary of object, and the cells' size changes gradually, as shown in Fig. 3.

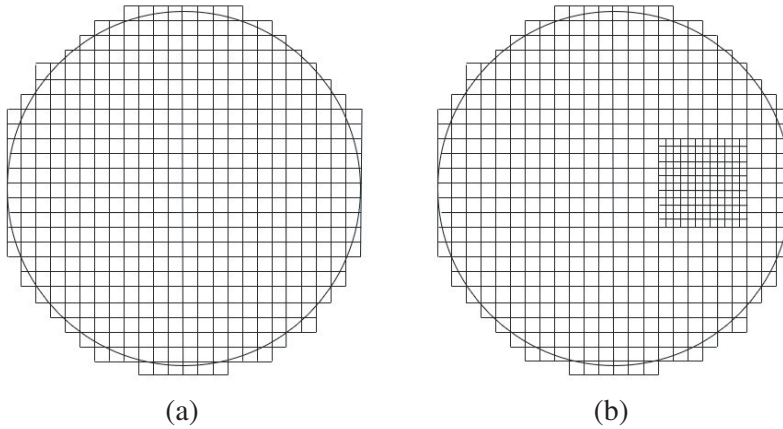


**Figure 2.** Rectangular mesh results for (a) uni-mesh and (b) dual-mesh scheme.

Based on [20], any set of points in the  $x$ - $y$  plane can be triangulated by the Delaunay algorithm. For a triangular cell, the bar which is the edge of the triangle cell has a force displacement relationship described by  $f(l, l_0)$ , which depends on its current length  $l$  and its unextended length  $l_0$ . The external forces on the structure come at the boundaries. At every boundary node, there is a reaction force acting normal to the boundary. The positions of the joints are found by solving for a static force equilibrium in the structure. As the lengths of all the bars at equilibrium will be nearly equal, we can get a well-shaped triangular mesh. For the 2-D situation [20], the force vector is given as

$$F(r) = [F_{\text{int},x}(r) \ F_{\text{int},y}(r)] + [F_{\text{ext},x}(r) \ F_{\text{ext},y}(r)] \quad (7)$$

where  $F_{\text{int}}$  contains the internal forces from the bars, and  $F_{\text{ext}}$  are the external forces, which act from the boundaries. In addition,  $r$  is an  $N \times 2$  array, containing  $x$  and  $y$  component values.

Equation (7) is then solved for a set of equilibrium positions  $r$ . In [20], the desired edge length distribution is provided by the user as an element size function  $h(x, y)$ . It gives the relative distribution

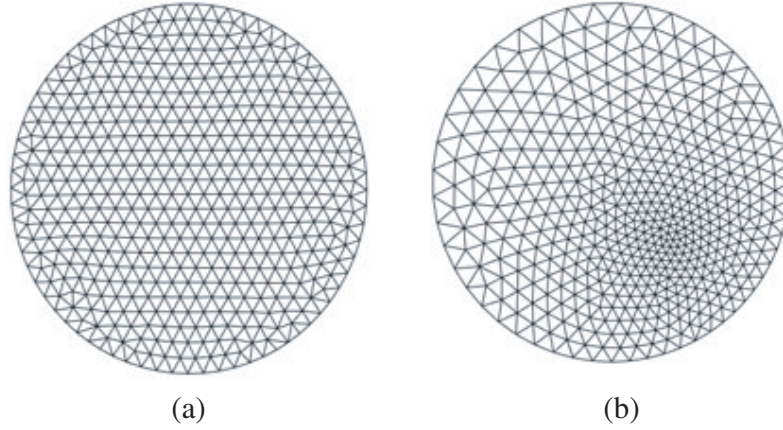


**Figure 3.** Distmesh results for (a) uni-mesh and (b) dual-mesh scheme.

over the domain. To find the scaling factor SF, we compute the ratio between the mesh area from the actual edge length  $l_i$  and the desired size using

$$SF = \left( \frac{\sum l_i^2}{\sum h(x_i, y_i)^2} \right)^{1/2} \quad (8)$$

where  $h(x, y)$  is specified by the user, or it could also be created using adaptive logic to implement the local feature size, which is roughly the distance between the boundaries of the region.

### 3. THE COSAMP RECONSTRUCTION ALGORITHM

Compressive sensing deals with an incomplete linear equations, which projects the original signal onto a set of measurement vector, as shown in Equation (9),

$$y = \Phi s \quad (9)$$

where  $\Phi$  is an  $M \times N$  matrix and called the measurement matrix;  $s$  is the processed signal with length  $N$ ; and  $y$  is the measurement vector of size  $M$ . Combining with the discussion in Section 2, in 2-D microwave reconstruction process, the measurement matrix  $\Phi$  is formed by Green's functions  $G^r$ ,  $G^s$ , incident field  $E_l^i$ , and contrast complex permittivity function  $\Delta\epsilon$ . Also,  $y$  represents the measured data of scattered field in vector form.

In the compressive sensing method, to solve the incomplete linear equation in Equation (9), the unknown vector is required to have few nonzero entries relative to its dimension. Especially for a non-sparse object, we need to introduce sparsity into the original signal. As a result, an appropriate transformation method to transfer the non-sparse signal to a domain where it can be represented by a sparse signal needs to be applied before the compressive sensing process. In this paper, we choose non-decimated wavelet transformation to process the original signal beforehand to induce sparsity in the signal in the wavelet domain. The transformation process is described as

$$s = \Psi x \quad (10)$$

where  $\Psi$  is known as the wavelet transformation dictionary.

Then, the reformulation result of the linear equation is described as

$$y = \Phi \Psi x = Ax \quad (11)$$

where  $A = \Phi \Psi$ . Based on Equation (11), further compressive sensing process operates on the sparser signal  $x$  generated by ND-wavelet transformation matrix, instead of operating on the original input signal  $s$ .

### 3.1. Non-Decimated Wavelet Transformation

Based on [23], with an assumption that a multiresolution framework is specified,  $\phi$  and  $\psi$  are denoted as the scaling and wavelet functions, respectively. A data vector  $y = (y_0, y_1, \dots, y_{m-1})$  of size  $m$  forms a function  $f$  in terms of shifts of the scaling function at some multiresolution level  $J$  such that  $J - 1 < \log_2 m \leq J$ , as

$$f(x) = \sum_{k=0}^{m-1} y_k \phi_{J,k}(x) \quad (12)$$

where  $\phi_{J,k}(x) = 2^{J/2} \phi(2^J(x - k))$ . The data interpolating function  $f$  can be represented as

$$f(x) = \sum_{k=0}^{m-1} c_{J_0,k} \phi_{J_0,k}(x) + \sum_{j=J_0}^{J-1} \sum_{k=0}^{m-1} d_{jk} 2^{j/2} \psi_{jk}(2^j(x - k)) \quad (13)$$

where

$$\phi_{J_0,k}(x) = 2^{J_0/2} \phi(2^{J_0}(x - k)) \quad (14)$$

and

$$\psi_{jk}(x) = 2^{j/2} \psi(2^j(x - k)) \quad (15)$$

Coefficients  $c_{J_0,k}$  and  $d_{jk}$  represent the NDWT of vector  $y$ , wherein coefficient  $c_{J_0,k}$  serves as the coarsest approximation of the data, and  $d_{jk}$  serves as the detail coefficients.  $J_0$  is the coarsest decomposition level. For a 2-D signal of size  $m \times n$ ,  $p_1$  and  $p_2$  level decompositions along rows and columns are obtained by NDWT matrix multiplication from the left and its transpose from the right. When expressing the NDWT in matrix form, the transform results in a 2-D signal  $B$  of size  $(p_1 + 1)m \times (p_2 + 1)n$ . Hence the NDWT matrix form can be summarized as shown in Equations (16) and (17),

$$B = W_m^{p_1} \times A \times W_m^{p_2'} \quad (16)$$

$$A = W_m^{p_1'} \times T_m^{p_1} \times B \times T_m^{p_2} \times W_m^{p_2} \quad (17)$$

where  $A$  is the original signal matrix, and  $B$  is the wavelet transformation result.  $T_m^{p_1}$ ,  $T_m^{p_2}$  are the rescaling matrices.  $W_m^{p_1}$  and  $W_m^{p_2}$  could be constructed by different wavelet filters, and  $W_m^{p_2'}$  and  $W_m^{p_1'}$  are the complex conjugates of matrices  $W_m^{p_2}$  and  $W_m^{p_1}$ , respectively.

### 3.2. Introduction of the CoSaMP Algorithm

The CoSaMP algorithm is developed based on the Orthogonal Matching Pursuit (OMP) algorithm, which belongs to the greedy pursuit algorithms category. However, the CoSaMP algorithm combines some enhanced ideas compared to the OMP, such as selecting multiple columns per iteration, pruning the columns at each step, solving the least squares problem iteratively, and using the restricted isometry property (RIP) bound. The CoSaMP algorithm selects the  $K$  largest entries of a vector by applying a pseudoinverse to the measurement vector with a hard thresholding [19].

The CoSaMP algorithm starts with initializing all the parameters in the algorithm. During each iteration, we identify columns of  $A$  that are most strongly correlated with the proxy residual  $\tilde{v}$ . Then, we merge the old and new columns into one set to obtain a new set, denoted as  $T$ . After that, we find the best coefficients for approximating the residual with these columns. We retain the  $k$  largest coefficients and update the residual  $r$ . The iteration process runs until the stopping criterion holds, and we obtain the approximate value  $\hat{x}$ . The entire process is summarized in Fig. 4.

Reference [28] indicates that both the algorithm performance and theoretical analysis of CoSaMP require the measurement matrix  $A$  to satisfy the RIP with a sufficiently small constant  $\delta_k \in (0, 1)$ , which is described as

$$\sqrt{1 - \delta_k} \leq \frac{\|\Phi s\|_2}{\|s\|_2} \leq \sqrt{1 + \delta_k} \quad (18)$$

This condition would not perform well when the dictionary is our chosen ND-Wavelet transformation matrix, as it is not unitary and highly redundant.

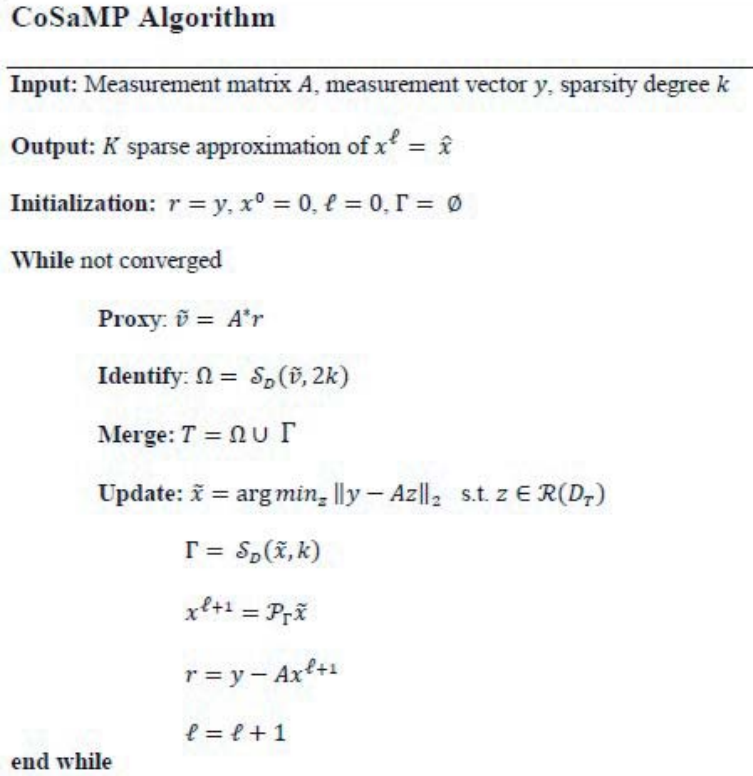


Figure 4. CoSaMP algorithm calculation process.

As we apply wavelet transformation dictionary  $\Psi$  to introduce the sparsity, the RIP of order  $k$  is given as

$$\sqrt{1 - \delta_k} \leq \frac{\|\Phi\Psi x\|_2}{\|\Psi x\|_2} \leq \sqrt{1 + \delta_k} \tag{19}$$

with all  $x$  satisfying  $\|x\|_0 \leq k$ . This modified CoSaMP requires relatively weaker assumptions and the  $k$ -RIP condition, which is a different and less-restrictive condition than requiring  $\Phi\Psi$  to satisfy the RIP condition.

### 3.3. Regularization Matrix

Based on the forward problem discussion in Section 2, the forward calculation results correspond to the size of the cell size. With the introduction of different cell sizes, especially, the smaller size cells containing more important information for the user, we need to compensate the forward calculation process to prevent these elements from being eliminated by the hard threshold in early stages. For this purpose, a regularization matrix  $B$  is introduced into the forward calculation before the wavelet transformation, which is given as

$$B = \text{diag} \left( \frac{f(\Theta)}{f(\max(\Theta))} \right) \tag{20}$$

where  $\Theta$  is a vector of area for all cells;  $\max(\cdot)$  stands for the operation of choosing the maximum value of a vector;  $\text{diag}(\cdot)$  is a function to fill vectors to the diagonal elements of a matrix; and  $f(\cdot)$  presents the operation we choose to preprocess the elements' area. In this paper, different  $f(\cdot)$  operations  $S$  are chosen to compare their performances in Section 4.

Based on [16, 29], the introduction of the regularization matrix  $B$  is able to avoid the error during MoM calculation due to different cell sizes and enhance  $S$  the convergence of the CoSaMP algorithm. After we obtain the reconstructed signal, the inverse of matrix  $B$  is applied to the reconstructed result

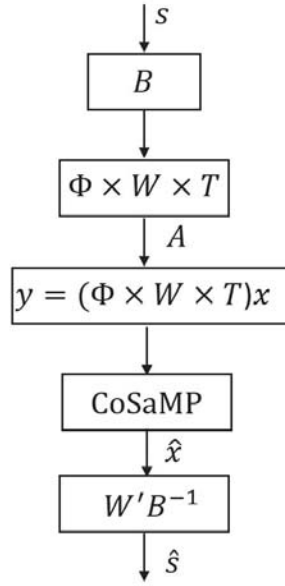


**Figure 5.** CoSaMP algorithm with regularization matrix calculation flow.

to recover the original signal  $x$  in Equation (10). The complete process of the algorithm is shown in the block diagram in Fig. 5. In Fig. 5, blocks  $B$  and  $B^{-1}$  are the regularization operations for the forward problem.  $W \times T$  and  $W^*$  blocks describe the ND-wavelet transformation and inverse ND-wavelet transformations, respectively.

#### 4. RESULTS AND DISCUSSION

In this section, three numerical experiment results are presented to demonstrate the performance of our algorithm: (1) the CoSaMP reconstruction results with different selected regularization matrices. In this part, results from different regularization matrices and result from the non-regularized matrix are compared; (2) the reconstruction of circular phantom with different CoSaMP hard threshold values; (3) the reconstruction comparison between conventional OMP method and our proposed modified dual-mesh CoSaMP method with inhomogeneous synthetic data.

The synthetic data used in the first two experiments are collected from the full-wave solver CST studio. All of the circular phantoms are placed in  $x$ - $y$  plane and oriented along  $z$ -axis. The simulation boundary along  $z$ -axis is assumed to follow the perfect electrical conductor boundary condition, whereas all the other boundaries are set up as open conditions. The incident EM fields are generated by a current source along the  $z$ -axis with an amplitude equal to 1 A. Probes along  $z$ -oriented direction are placed on the edge of image domain to act as antenna receivers. All the setups described above are to collect 2-D TM polarized synthetic data from CST.

##### 4.1. Case 1: Modified CoSaMP Algorithm with Different Regularization Matrix

A non-sparse model containing two dielectric circular cylinders is reconstructed by modified dual-mesh CoSaMP methods at a frequency of 403.5 MHz. The chosen frequency needs to balance the penetration depth and minimum cell size based on [1]. As introduced in Section 2, the image domain denoted by  $\mathcal{S}$  is a circular region with radius 60 cm. The image domain is filled with background material which has the parameters  $\epsilon_r = 55$  at 403.5 MHz. Transmitters and receivers are placed along the image domain at equal intervals of  $5^\circ$ . As a result, the total number of receivers is  $M = 71$ , and number of source rotation positions is  $N = 72$ . During each scan, the transmitter is placed at one of the receiver position, and the remaining 71 receivers receive the total field signal. After the transmitter rotates 72 times, we obtain a data matrix of size  $72 \times 71$ .

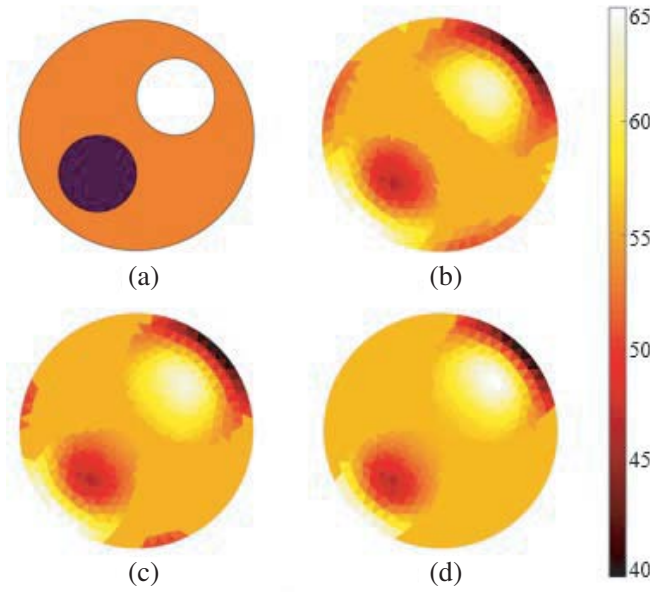


**Figure 6.** Dual-mesh scheme CoSaMP algorithm reconstruction results with circular synthetic phantom. (a) Initial inhomogeneous circular phantom. (b) Dual-mesh modified CoSaMP algorithm reconstruction result without regularization matrix. (c) Dual-mesh modified CoSaMP algorithm reconstruction result with first order regularization matrix. (d) Dual-mesh modified CoSaMP algorithm reconstruction result with second order regularization matrix.

The circular phantom is shown in Fig. 6(a), where the radius of both dielectric cylinders is 20 mm. The white cylinder has relative permittivity value  $\epsilon_r = 60$ , and the brown cylinder has  $\epsilon_r = 48$ . Applying Distmesh method for dual-mesh discretization, the denser cells are clustered around the center of the image domain. The image domain is discretized by 998 elements in this simulation. The reconstruction result without applying regularization matrix is shown in Fig. 6(b).

The first regularization operation  $f(\cdot)$  is chosen as identical operation, which is called first order operation. Then, Equation (20) is specified as

$$B = \text{diag} \left( \frac{\Theta}{\max(\Theta)} \right) \quad (21)$$

Furthermore, the second version of  $f(\cdot)$  is selected as second order operation. The expression for the regularization matrix is presented as

$$B = \text{diag} \left( \frac{\Theta^2}{(\max(\Theta))^2} \right) \quad (22)$$

The reconstruction results are shown in Fig. 6. The image domain is divided into 998 cells with different sizes. The area closer to the center of image domain has denser mesh grid, and the cells close to the boundary have a coarser mesh grid. All the results presented in Fig. 6 have the same  $k = 450$  values. Fig. 6(b) presents the reconstruction result with CoSaMP algorithm without our regularization matrix. Although our algorithm with dual-mesh scheme is able to recover the dielectric profile in the image domain, the noise around the boundary of the image domain is excessive. Fig. 6(c) presents the reconstruction results with first order regularization matrix. The result shows less noise element recovered by introducing our regularization matrix. In addition, the area close to center, which contains smaller cells, has more cells recovered, and the result is closer to the original circular phantom. Fig. 6(d) shows the second order regularization matrix reconstruction result. This result shows that all the recovered cells are related to our two small cylinders in the image domain. Furthermore, the reconstruction result is cleaner than the result without regularization and use of the first order regularization matrix.

It is easy to conclude that the second order regularization matrix leads to a better reconstruction result. As shown in Section 2, during the forward calculation, the dielectric profile is modeled using Green's function. The cell size is involved in the calculation of the Green's function in Equations (5) and (6). As a result, the second order regularization matrix compensates the forward solving process better.

#### 4.2. Case 2: Reconstruction of Inhomogeneous Dielectric Circular Cylinders Against Simulated Data with OMP Algorithm and Modified CoSaMP Algorithm

In the second numerical experiment, the synthetic data are collected under the same conditions as Case 1. In this case, the same synthetic data are reconstructed by two different algorithms: OMP and proposed CoSaMP algorithms, respectively.

The reconstruction results from OMP and CoSaMP algorithms are shown in Fig. 7. The first column, namely, Figs. 7(a), (c), and (e), present the reconstruction result from CoSaMP algorithm without regularization matrix, with first order and with second order regularization matrix, respectively. The second column, namely Figs. 7(b), (d), and (f) show the same content but for the OMP algorithm. From each pairwise comparison, we can infer that the CoSaMP algorithm generally performs better than the OMP algorithm, as the values in certain cells are recovered closer to that of the original phantom, and the number of non-relative elements recovered is less.

Next, we also compare the robustness to noise of the OMP and the CoSaMP algorithms. Different

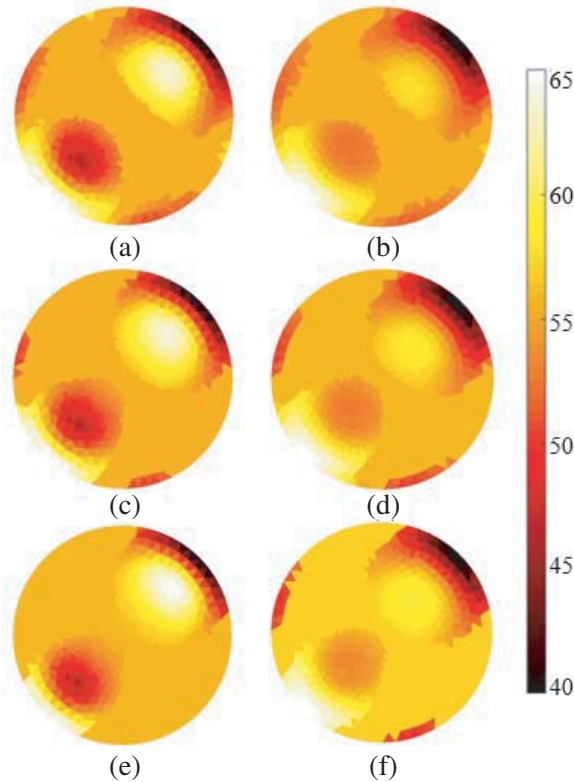


**Figure 7.** Circular phantom reconstructed with dual-mesh CoSaMP and OMP algorithms. (a) Dual-mesh modified CoSaMP algorithm reconstruction result without regularization matrix. (b) Dual-mesh modified OMP algorithm reconstruction result without regularization matrix. (c) Dual-mesh modified CoSaMP algorithm reconstruction result with first order regularization matrix. (d) Dual-mesh modified OMP algorithm reconstruction result with first order regularization matrix. (e) Dual-mesh modified CoSaMP algorithm reconstruction result with second order regularization matrix. (f) Dual-mesh modified OMP algorithm reconstruction result with second order regularization matrix.

amounts of white Gaussian noise, at signal-to-noise ratios (SNRs) of 0, 5, and 10 dB, are added to the scattered data. The noise added to the data signal corresponds to the power of measured signal at the receivers. The noise added to the measurement signal is calculated as

$$P_{\text{noise}} = \frac{1}{M} \sum_{i=1}^M |E_{\text{meas},i}^{\text{scatt}}|^2 \quad (23)$$

where  $E_{\text{meas},i}^{\text{scatt}}$  is the measured scattered data at the  $i$ -th receiver. The additive white Gaussian noise is given by

$$n = \sqrt{\frac{P_{\text{noise}}}{2}}(n_1 + jn_2) \quad (24)$$

where  $n_1$  and  $n_2$  are two Gaussian distributed random variables.

The reconstruction results are shown in Fig. 8. Both the OMP and CoSaMP algorithms are able to recover signal when the SNR equals 10 dB. The CoSaMP algorithm performs a little better at high SNR value of 10 dB, as shown in Figs. 8(a), (b). However, as the SNR values decrease to 5 and 0 dB, both algorithms struggle to recover the image. The non-relative noise appearing around the image domain boundary increases. When SNR drops to 0 dB, the OMP algorithm is not able to reconstruct

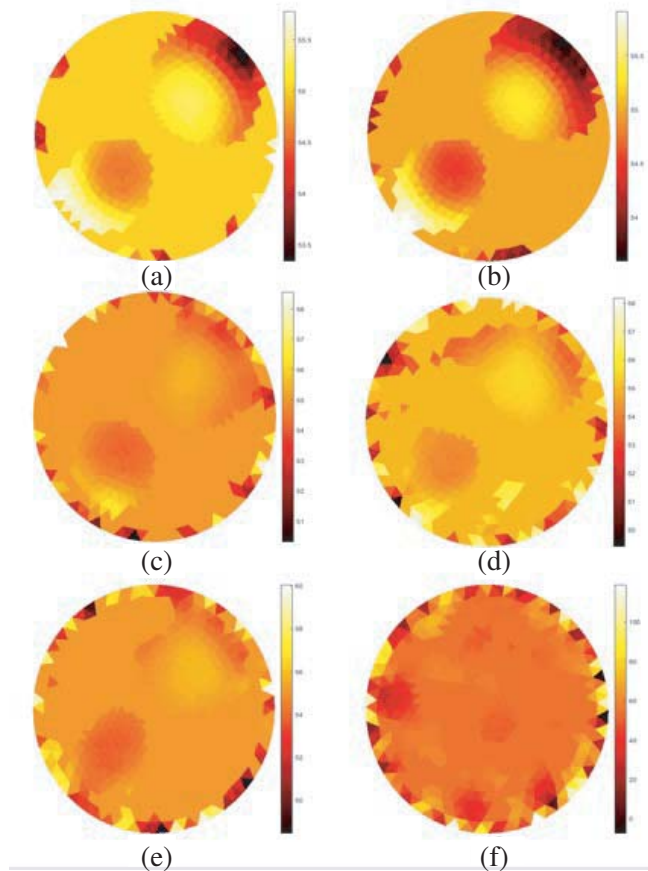


**Figure 8.** CoSaMP and OMP algorithm reconstruction results with different signal-to-noise ratios (SNRs) 10 dB, 5 dB and 0 dB, respectively. (a) CoSaMP method reconstruction results at 10-dB SNR level. (b) OMP method reconstruction results at 10-dB SNR level. (c) CoSaMP method reconstruction results at 5-dB SNR level. (d) OMP method reconstruction results at 5-dB SNR level. (e) CoSaMP method reconstruction results at 0-dB SNR level. (f) OMP method reconstruction results at 0-dB SNR level.

a reasonable image. However, the CoSaMP algorithm is still able to recover a heavily distorted image. The noise around boundary grows bigger and stronger.

Furthermore, the normalized residual  $\hat{r}$  of the algorithm is defined as

$$\hat{r} = \frac{\|y - A\hat{x}\|_2}{\|y\|_2} \quad (25)$$

Here, combined with forward scattering model, the normalized residual is presented as

$$\hat{r} = \frac{\|E_{\text{meas}}^{\text{scatt}} - A\widehat{E}_{\text{recon}}^{\text{scatt}}\|_2}{\|E_{\text{meas}}^{\text{scatt}}\|_2} \quad (26)$$

where  $E_{\text{recon}}^{\text{scatt}}$  is the recovered scattered field at end of the algorithm process, and  $E_{\text{meas}}^{\text{scatt}}$  is the measured scattered data (in this simulation, it is related to the synthetic data). The normalized residuals are shown in Table 1.

**Table 1.** Normalized residual.

| SNR   | CoSaMP | OMP               |
|-------|--------|-------------------|
| 10 dB | 0.089  | 0.102             |
| 5 dB  | 0.218  | 0.436             |
| 0 dB  | 0.524  | Does not converge |

### 4.3. Case 3: Reconstruction Result with Fresnel Experimental Data

In this experiment, we apply our proposed algorithm to practical data from the Institute Fresnel, Marseille. The experimental measurement setup has been described in [30]. The data we selected are TM-polarized FoamDielExt, FoamDielInt [30]. As shown in Fig. 9(a) and Fig. 10(a), the white cylinder represents plastic with relative permittivity  $\varepsilon_r = 3 \pm 0.3$ , and the gray area represents foam with relative permittivity  $\varepsilon_r = 1.45 \pm 0.15$ . Based on the description in [25], all the cylinders inside the image domain are 1.5 m long and modelled as infinitely long to obtain 2-D TM data.

The image domain  $\mathcal{S}$  is set up in a shape of a square of  $0.15 \times 0.15 \text{ m}^2$  size, and centered at origin of the  $x$ - $y$  plane. In our simulation, the center of the plastic cylinder is chosen as the center of the

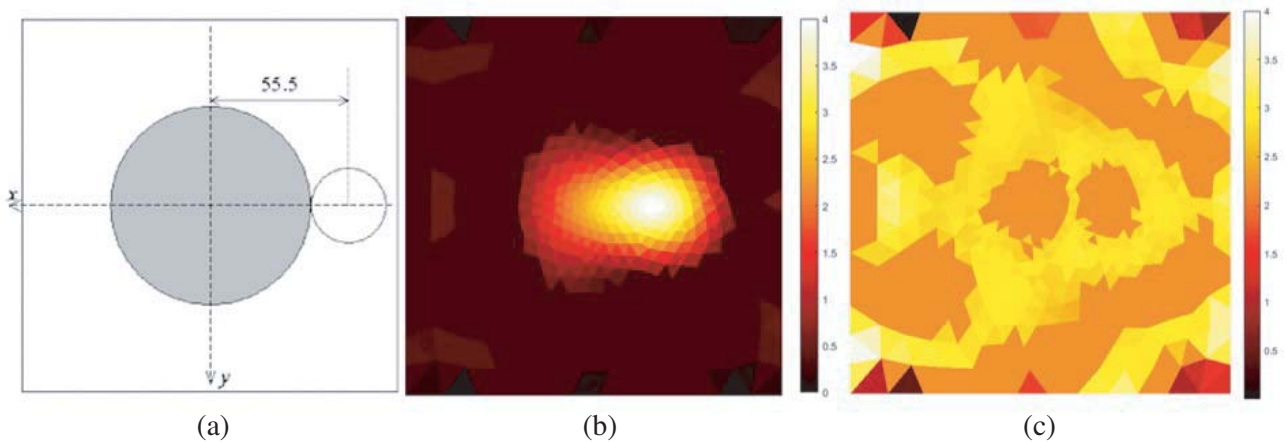


**Figure 9.** (a) Experiment object setup description of FoamDielExt [30]. (b) Reconstruction results from modified CoSaMP algorithm with regularization matrix. (c) Reconstruction results from modified CoSaMP algorithm without regularization matrix.

denser mesh. After dual-mesh discretizes the image domain, we get cell number 986 in total. In the simulation, the hard threshold value is set as 450.

Figure 9 shows the reconstruction results of the relative permittivity using FoamDielExt data. Fig. 10 shows the reconstruction results of the relative permittivity using FoamDielInt data. Fig. 9(b) and Fig. 10(b) present the reconstruction results of modified CoSaMP algorithm with second order regularization matrix. Fig. 9(c) and Fig. 10(c) show the recovery modified CoSaMP algorithm without regularization matrix. Both experiments show that the regularization matrix helps to reconstruct the dielectric profile better. However, compared to our synthetic data, the noise in non-object area is more obvious. This is due to the nonlinear level of the practical data and the threshold number we selected.

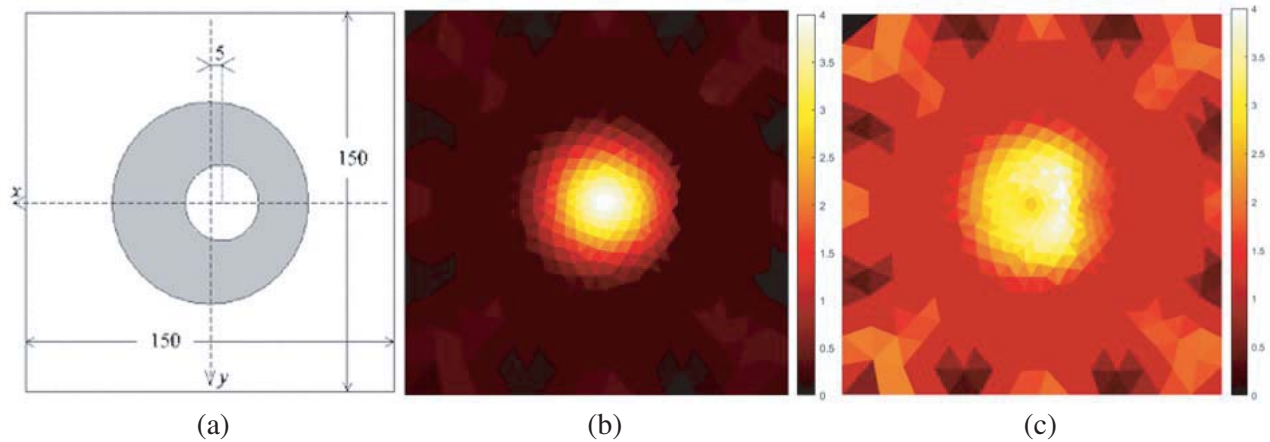


**Figure 10.** (a) Experiment object setup description of FoamDielInt [30]. (b) Reconstruction results from modified CoSaMP algorithm with regularization matrix. (c) Reconstruction results from modified CoSaMP algorithm without regularization matrix.

## 5. CONCLUSIONS

In this paper, a novel microwave reconstruction imaging method using dual-mesh method and signal space Compressive Sampling Matching Pursuit (CoSaMP) has been proposed and tested. In addition, with the introduction of the different sizes of discretized cells, a regularization matrix is proposed to compensate its effect and to help improve the convergence and robustness of our algorithm. To demonstrate the method performance, three experiments utilizing synthetic data and real experimental data are presented. From the results and analysis above, the proposed method is able to reconstruct the image of a non-sparse object. In addition, compared to other algorithms, our method is faster and more robust. In the future, we will work on the analysis of relationship between the CoSaMP algorithm threshold and number of receivers. We also plan to collect more practical data and employ our method in other applications, such as ground penetration radar imaging and through-barrier imaging. In addition, we plan to perform deeper research on the dual mesh method benefit on algorithm convergence behavior. Specifically, we intend to compare the triangular discretized method to the traditional rectangular mesh grid and plot the convergence performance of the two methods. These results will be communicated in the future.

## REFERENCES

1. Chandra, R., H. Zhou, I. Balasingham, and R. M. Narayanan, "On the opportunities and challenges in microwave medical sensing and imaging," *IEEE Transactions on Biomedical Engineering*, Vol. 62, No. 7, 1667–1682, 2015.

2. Zhou, H., R. Narayanan, I. Balasingham, and R. Chandra, "Radar for disease detection and monitoring," *Radar for Indoor Monitoring: Monitoring: Detection, Localization and Assessment*, edited by M. G. Amin, 301–335, CRC Press, Boca Raton, FL, 2017.
3. Chandra, R., H. Zhou, I. Balasingham, and R. M. Narayanan, "Medical microwave imaging and analysis," *Medical Image Analysis and Informatics: Computer-Aided Diagnosis and Therapy*, P. M. de Azevedo-Marques, A. Mencattini, M. Salmeri, and R. M. Rangayyan (eds.), 451–466, CRC Press, Boca Raton, FL, 2018.
4. Colton, D. L. and R. Kress, *Inverse Acoustic and Electromagnetic Scattering Theory*, Springer-Verlag, Berlin, 1992.
5. Franchois, A. and C. Pichot, "Microwave imaging-complex permittivity reconstruction with a Levenberg-Marquardt method," *IEEE Transactions on Antennas and Propagation*, Vol. 45, No. 2, 203–215, 1997.
6. Hohage, T., "Logarithmic convergence rates of the iteratively regularized Gauss-Newton method for an inverse potential and an inverse scattering problem," *Inverse Problems*, Vol. 13, No. 5, 1279–1299, Jan. 1997.
7. Zhou, H., R. M. Narayanan, R. Chandra, and I. Balasingham, "Microwave imaging of circular phantom using the Levenberg-Marquardt method," *Proc. SPIE Conf. Radar Sensor Technology XIX and Active and Passive Signatures VI*, Baltimore, MD, Apr. 2015, doi: 10.1117/12.2176754.
8. Van Den Berg, P. M. and A. Abubakar, "Contrast source inversion method: State of art," *Progress In Electromagnetics Research*, Vol. 34, 189–218, 2001.
9. Li, L., H. Zheng, and F. Li, "Two-dimensional contrast source inversion method with phaseless data: TM case," *IEEE Transactions on Geoscience and Remote Sensing*, Vol. 47, No. 6, 1719–1736, 2009.
10. Hajihashemi, M. R. and M. El-Shenawee, "Shape reconstruction using the level set method for microwave applications," *IEEE Antennas and Wireless Propagation Letters*, Vol. 7, 92–96, 2008.
11. Irishina, N., D. Álvarez, O. Dorn, and M. Moscoso, "Structural level set inversion for microwave breast screening," *Inverse Problems*, Vol. 26, No. 3, 035015, 2010.
12. Candes, E. and M. Wakin, "An introduction to compressive sampling," *IEEE Signal Processing Magazine*, Vol. 25, No. 2, 21–30, 2008.
13. Pati, Y. C., R. Ramin, and P. S. Krishnaprasad, "Orthogonal matching pursuit: Recursive function approximation with applications to wavelet decomposition," *Proc. 27th Asilomar Conference on Signals, Systems and Computers*, 40–44, Pacific Grove, CA, Nov. 1993.
14. Davis, G., S. Mallat, and M. Avellaneda, "Adaptive greedy approximations," *Constructive Approximation*, Vol. 13, No. 1, 57–98, 1997.
15. Azghani, M., P. Kosmas, and F. Marvasti, "Microwave medical imaging based on sparsity and an iterative method with adaptive thresholding," *IEEE Transactions on Medical Imaging*, Vol. 34, No. 2, 357–365, 2014.
16. Zhou, H. and R. M. Narayanan, "Microwave imaging of nonsparse object using dual-mesh method and iterative method with adaptive thresholding," *IEEE Transactions on Antennas and Propagation*, Vol. 67, No. 1, 504–512, 2019.
17. Blumensath, T. and M. E. Davies, "Iterative thresholding for sparse approximations," *Journal of Fourier Analysis and Applications*, Vol. 14, Nos. 5–6, 629–654, 2008.
18. Blumensath, T. and M. E. Davies, "Iterative hard thresholding for compressed sensing," *Applied and Computational Harmonic Analysis*, Vol. 27, No. 3, 265–274, 2009.
19. Needell, D. and J. A. Tropp, "CoSaMP: Iterative signal recovery from incomplete and inaccurate samples," *Applied and Computational Harmonic Analysis*, Vol. 26, No. 3, 301–321, 2009.
20. Persson, P.-O., "Mesh size functions for implicit geometries and PDE-based gradient limiting," *Engineering with Computers*, Vol. 22, No. 2, 95–109, 2006.
21. Zhou, H., R. M. Narayanan, and I. Balasingham, "Microwave reconstruction method using a circular antenna array cooperating with an internal transmitter," *Proc. SPIE Conf. Radar Sensor Technology XX*, Baltimore, MD, Apr. 2016, doi: 10.1117/12.2228287.

22. Paulsen, K., P. Meaney, M. Moskowitz, and J. Sullivan, "A dual-mesh scheme for finite element based reconstruction algorithms," *IEEE Transactions on Medical Imaging*, Vol. 14, No. 3, 504–514, 1995.
23. Brassarote, G. O. N., E. M. Souza, and J. F. G. Monico, "Non-decimated wavelet transform for a shift-invariant analysis," *Tendências em Matemática Aplicada e Computacional*, Vol. 19, No. 1, 93–110, 2018.
24. Loboda, N. S., A. V. Glushkov, V. N. Khokhlov, and L. Lovett, "Using non-decimated wavelet decomposition to analyse time variations of North Atlantic oscillation, eddy kinetic energy, and Ukrainian precipitation," *Journal of Hydrology*, Vol. 322, Nos. 1–4, 14–24, 2006.
25. Balanis, C. A., *Advanced Engineering Electromagnetics*, J. Wiley & Sons, Hoboken, NJ, 2012.
26. Chandra, R., A. J. Johansson, M. Gustafsson, and F. Tufvesson, "A microwave imaging-based technique to localize an in-body RF source for biomedical applications," *IEEE Transactions on Biomedical Engineering*, Vol. 62, No. 5, 1231–1241, 2015.
27. Chew, W. and Y. Wang, "Reconstruction of two-dimensional permittivity distribution using the distorted Born iterative method," *IEEE Transactions on Medical Imaging*, Vol. 9, No. 2, 218–225, 1990.
28. Davenport, M. A., D. Needell, and M. B. Wakin, "Signal space CoSaMP for sparse recovery with redundant dictionaries," *IEEE Transactions on Information Theory*, Vol. 59, No. 10, 6820–6829, 2013.
29. Sandhu, A. I. and H. Bagci, "A modified CoSaMP algorithm for electromagnetic imaging of two dimensional domains," *Proc. 2017 International Applied Computational Electromagnetics Society Symposium-Italy (ACES)*, Florence, Italy, Mar. 2017, doi: 10.23919/ROPACES.2017.7916412.
30. Geffrin, J.-M., P. Sabouroux, and C. Eyraud, "Free space experimental scattering database continuation: Experimental set-up and measurement precision," *Inverse Problems*, Vol. 21, No. 6, S117–S130, 2005.